Journal of Colloid and Interface Science 690 (2025) 137281

Contents lists available at ScienceDirect

Journal of Colloid And Interface Science

journal homepage: www.elsevier.com/locate/jcis

Regular Article

Nature of oxygen vacancy in accelerating redox kinetics of V^{2+}/V^{3+} in flow batteries

Rongjiao Huang [a], Shuhao Su [a], Yincheng Wang [a], Suqin Liu [b,*], Zhen He [b], Li Tian [a], Dong Luo [a], Haikun Xu [c], Jue Wang [b,*]

[a] School of Materials Science and Engineering, Hunan Provincial Key Laboratory of Advanced Materials for New Energy Storage and Conversion, Hunan University of Science and Technology, Xiangtan, Hunan 411201, PR China
[b] College of Chemistry and Chemical Engineering, Central South University, Changsha, Hunan 410083, PR China
[c] Information and Network Center, Central South University, Changsha, Hunan 410083, PR China

HIGHLIGHTS

- TiO_2 nanoplates with adjustable oxygen vacancy concentration were synthesized via a low-temperature annealing strategy.
- A strong correlation between the oxygen vacancy concentration and the catalytic activity toward V^{2+}/V^{3+}.
- Enhanced activity of V^{2+}/V^{3+} stems from the optimized desorption and electron transfer process during the oxidation process.
- The nature of oxygen vacancy boosting the redox kinetics of V^{2+}/V^{3+} was disclosed.

GRAPHICAL ABSTRACT

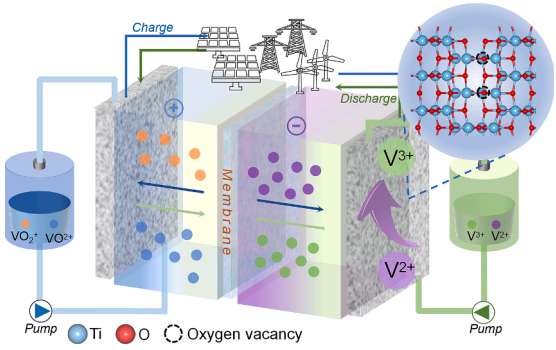

ARTICLE INFO

Keywords:
Oxygen vacancy concentration
Reaction kinetics
Catalytic mechanism
Electrode
Redox flow batteries

ABSTRACT

The rational design of oxygen vacancy in metal oxide based catalysts is an effective strategy to enhance their intrinsic activity by influencing the microelectronic structure. However, the impact of oxygen vacancy on the reaction kinetics and the catalytic mechanism in vanadium redox flow batteries (VRFBs) remains under-explored. Herein, a novel approach is developed to regulate the concentration of oxygen vacancy in TiO_2 nanoplates for high performance VRFBs. The oxygen vacancy-rich TiO_2 efficiently facilitates the desorption and electron transfer process of V^{3+} during the electrochemical oxidation process. Owing to the enhanced electrochemical oxidation of V^{2+} to V^{3+}, the inherently sluggish reaction kinetics of V^{2+}/V^{3+} is significantly accelerated. The battery assembled with oxygen vacancy-rich TiO_2 achieves an energy efficiency of 79.81 % at 200 mA cm^{-2} and outstanding long-term durability. This work not only elucidates the nature of oxygen vacancy in accelerating the redox kinetics of V^{2+}/V^{3+} but also offers insights for rationally designing efficient catalysts for VRFBs.

* Corresponding authors.
E-mail addresses: sqliu2003@126.com (S. Liu), jwang79@crimson.ua.edu (J. Wang).

https://doi.org/10.1016/j.jcis.2025.137281
Received 20 December 2024; Received in revised form 5 March 2025; Accepted 8 March 2025
Available online 9 March 2025

1. Introduction

The large-scale energy storage is essential for the widespread application of intermittent renewable energy, such as wind and solar power [1,2]. Vanadium redox flow battery (VRFB) is one of the most promising candidates for the large-scale energy storage because of its flexible design, long lifespan, and low crossover contamination [3]. However, VRFB suffers from the low energy efficiency and low power density at a high current density, which is related to the commercial electrode of graphite felt (GF) that exhibits poor catalytic activity during redox reactions, particularly for the electrochemical redox of V^{2+}/V^{3+} [4].

Designing highly active catalysts loaded on the GF is an effective modification strategy to enhance the redox kinetics of V^{2+}/V^{3+} [5]. Metal oxide-based catalysts have garnered extensive research interest owing to their potential catalytic activity and low cost [6]. Nevertheless, the catalytic activity of metal oxide electrocatalysts remains below the desired standards for high performance VRFBs due to their poor electrical conductivity and insufficient intrinsic catalytic activity [7]. Introducing oxygen vacancies into metal oxide is promising to modulate its local electronic structure, thereby improving the inherent catalytic activity of the metal oxide [8]. Oxygen vacancies can affect the charge transfer process by regulating the band structure of metal oxides. Furthermore, oxygen vacancies can also serve as activation sites for reactant species, where the surface dangling bonds and localized electrons may alter the coordination environment of reactant species [9]. Consequently, oxygen vacancies play a vital role in the reaction kinetics and catalytic mechanisms of V^{2+}/V^{3+}.

Oxygen vacancies can be generated through hydrogen reduction or element doping [10–12]. Defect-rich CeO_2 nanowires were fabricated by hydrogen annealing, leading to a battery with an energy efficiency of 76.84 % at 80 mA cm^{-2} [13]. Sb-doped SnO_2 with increased oxygen vacancies exhibited an energy efficiency of 73.5 % at 150 mA cm^{-2} [12]. Additionally, some metal oxides feature oxygen vacancies due to their unique crystal structures, as seen in perovskites and high-entropy oxides [14]. Jiang et al. [15] explored the catalytic activity of $LaBO_3$ (B = V, Cr, Mn) perovskites towards V^{2+}/V^{3+} and VO^{2+}/VO_2^+ redox couples, of which oxygen vacancies in perovskites effectively promote the electron transfer of vanadium redox reactions. $LaBO_3$ decorated GF delivered an energy efficiency of 76.3 % at 150 mA cm^{-2}. Demeku et al. [16] introduced high-entropy oxide of $(BiZrMoWCeLa)O_2$ as a novel catalyst in VRFBs, highlighting its superior performance due to the rich oxygen vacancies. $(BiZrMoWCeLa)O_2$ demonstrated an energy efficiency of 73.34 % at 160 mA cm^{-2}.

As mentioned above, a broad consensus has emerged from prior research that oxygen vacancies exert a profound impact on the performance of VRFBs. However, the nature of oxygen vacancies in accelerating the reaction kinetics and the catalytic mechanism in VRFBs remains ambiguous. More importantly, the sluggish redox kinetics of V^{2+}/V^{3+} remain the bottleneck limiting the further improvement of VRFBs. The reported operating current density is typically below 200 mA cm^{-2}, which hinders the large-scale commercial application of VRFB. According to our previous research, the electrochemical oxidation of V^{2+} during the discharge process is the rate-determining step for V^{2+}/V^{3+} [17]. Therefore, the positively charged oxygen vacancies are promising to act as the electron accelerator, which selectively catalyzes the electrochemical oxidation process, thereby substantially improving the electrochemical performance of VRFBs, as schemed in Fig. 1. To address the aforementioned critical issues, it is vital to investigate the impact of oxygen vacancy concentration on the reaction kinetics and the catalytic mechanisms of V^{2+}/V^{3+}.

Herein, TiO_2 nanoplates with different oxygen vacancy concentration are fabricated via a low-temperature annealing strategy, showing promising potential for regulating the catalytic activity toward V^{2+}/V^{3+}. The impact of oxygen vacancy concentration on the redox kinetics of V^{2+}/V^{3+} is systematically investigated at different state of charge (SOC).

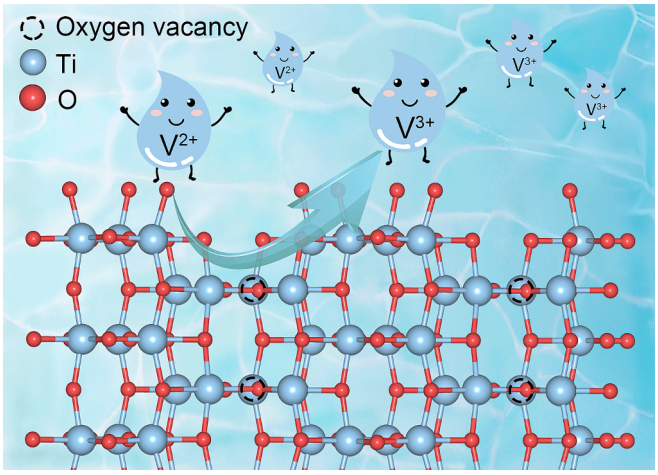

Fig. 1. The schematic illustration of the oxygen vacancy of TiO_2 accelerating the electrochemical oxidation process of V^{2+}/V^{3+}.

Oxygen vacancy-rich TiO_2 can specifically enhance the reaction kinetics of the rate-determining step of the V^{2+}/V^{3+}, i.e., the electrochemical oxidation of V^{2+} during the discharging process, thereby accelerating the V^{2+}/V^{3+} redox reaction. The in-depth theoretical calculations further reveal the influence of oxygen vacancy concentration on the catalytic mechanism of V^{2+}/V^{3+}. Oxygen vacancy-rich TiO_2 effectively promotes the V^{3+}desorption and the electron transfer process during the electrochemical oxidation of V^{2+}. Thus, VRFB assembled with oxygen vacancy-rich TiO_2 endows an exceptional energy efficiency of 74.39 % at a high current density of 300 mA cm^{-2} and excellent long-term durability. This work provides an effective strategy to address the bottleneck of VRFBs and elucidates the catalytic mechanism of oxygen vacancy concentration on V^{2+}/V^{3+}.

2. Methods

2.1. Materials

Tetrabutyl titanate ($Ti(OC_4H_9)_4$, Aladdin, 98 %), anhydrous ethanol (C_2H_5OH, Sinopharm, 95.0 %), and terephthalic acid ($C_8H_6O_4$, Aladdin, 99 %) were analytical grade and used without further purification. N, *N*-dimethylformamide (DMF, Sinopharm, 99.5 %), and anhydrous methanol (CH_3OH, Sinopharm, 99.5 %) were treated with 3A molecular sieves (Sinopharm) to remove the remaining moisture.

2.2. Synthesis of catalyst

2.2.1. Synthesis of MIL-125(Ti) precursor

MIL-125(Ti) was synthesized as follows [18]. 2.2 g of terephthalic acid was added into a solution of 36 mL of DMF and 4 mL of methanol, which were under stirring at room temperature for 30 min. 2.5 mL of Ti $(OC_4H_9)_4$ was added dropwise to the above solution under vigorous stirring. The solution was transferred into a 50 mL Teflon liner and heated at 150 ℃ for 33 h. Then the white precipitate was collected, washed by DMF and methanol for several times, and then dried at 60 ℃ for 12 h.

2.2.2. Synthesis of TiO_2 with different oxygen vacancy concentration

Oxygen vacancy-rich TiO_2 was synthesized by a low-temperature annealing strategy. 0.1 g MIL-125 (Ti) precursor was calcined in a muffle furnace at 400 °C for 3 h with a heating rate of 10 °C/min. Upon completion of the calcination, the sample was immediately extracted, and it was named TiO_2-400-10. Keeping all other preparation conditions constant, oxygen vacancy-deficient TiO_2 was prepared by adjusting the heating rate to 2 °C min^{-1}, named TiO_2-400-2. Additionally, under the

condition of a heating rate of 10 °C min^{-1}, the calcination temperature was controlled at 500 °C and 600 °C to regulate the oxygen vacancy concentration of the TiO_2. The samples were named TiO_2-500-10 and TiO_2-600-10, respectively.

2.3. Material characterization

The thermogravimetric analysis/derivative thermogravimetry (TG/DTG) was performed on a thermal analyzer (DTA-50) to characterize the decomposition processes of MIL-125 precursor from the room temperature to 700 °C in an Air atmosphere. Fourier transform infrared (FT-IR) spectrum in the range of 4000–400 cm^{-1} was characterized by Nicolet-5700 spectrometer. The crystalline structure of the samples was characterized by X-ray diffraction (XRD) by using Cu Kα (λ = 0.15418 nm) at a scan rate of 5° min^{-1} in the 2θ range of 5–90°. The morphology of the above materials was characterized by using a scanning electron microscope (SEM, JSM-7610F, JEOL™). The X-ray photoelectron spectroscopy (XPS) was carried out on a Thermo Fisher ESCALAB 250Xi spectrometer using an Al Kα source (1486.6 eV). Raman spectroscopy was tested on a Via-Reflex spectrometer (Renishaw) with a laser excitation wavelength of 532 nm. Electron paramagnetic resonance (EPR) was conducted by utilizing a Bruker EMXplus-10/12 instrument. The specific surface areas and pore diameter distributions were measured based on the N_2 adsorption–desorption isotherms (Micromeritics, ASAP 2020), using the Brunauer-Emmett-Teller (BET) to estimate specific surface area, and using the Barret-Joyner-Halenda (BJH) method to calculate the radial distributions of the pores and to perform mesoporous analysis. UV–vis spectra were conducted on a UV-2600 spectrometer (Shimadzu, Japan).

2.4. Electrochemical measurements

The electrochemical measurements were conducted by the typical three-electrode system in which an Ag/AgCl electrode (in saturated KCl) and a platinum mesh (1 cm^2) were used as the reference electrode and the counter electrode, respectively. A glassy carbon electrode (0.1963 cm^2) modified with the catalyst ink was selected as the working electrode. The catalyst ink was composed of 8 mg of catalyst, 950 μL of anhydrous ethanol, and 50 μL of 5 wt% Nafion dispersion (Dupont, USA). The catalyst ink was ultrasonically dispersed for at least half an hour. Then 8 μL of the uniformly dispersed ink was dripped on the glassy carbon electrode and dried in the air. The cyclic voltammetry (CV) and Tafel plots were measured on an Autolab PGSTAT204 electrochemical workstation. Electrochemical impedance spectroscopy (EIS) was performed on a CHI 660E electrochemical workstation in a frequency range of 0.1–100 kHz. The CV and EIS were carried out in the electrolyte containing 1.8 M V^{3+} + 3.6 M H_2SO_4. The Tafel plots and LSV were performed in a homemade electrochemical cell at a scan rate of 1 mV s^{-1} at 2025 rpm [17].

2.5. Flow battery test

VRFB was constructed using two graphite felts (Jin Gu Carbon Materials Co. Ltd., China, 4 cm × 4 cm × 4.3 mm) as the electrodes, with Nafion 212 (Dupont, USA) serving as the membrane and the graphite plate functioning as the bipolar plate. Both the initial positive and negative electrolyte consisted of 40 mL of 1.8 M $V^{3.5+}$ + 3.6 M H_2SO_4. For the oxygen vacancy-rich TiO_2 and oxygen vacancy-deficient TiO_2 modified batteries, all other components were identical except for the negative electrode.

The negative electrode was prepared as follows. The catalyst was dispersed in a mixture of 25 mL ethanol and 250 μL of 5 wt% Nafion solution and then uniformly distributed by sonication. The pristine graphite felt was immersed in the catalyst ink and subsequently dried at 60 °C in a vacuum drying oven. This process was repeated until the catalyst loading reached 3 mg cm^{-2}.

The charging and discharging test was conducted using a battery testing system (CT-4008, Neware Co., Ltd., China) at the current density from 150 to 400 mA cm^{-2} at room temperature. Galvanostatic intermittent titration technique (GITT) measurements were performed at 250 mA cm^{-2}. The voltage range was set between 0.9 V and 1.6 V, with the long-term stability carried out at 200 mA cm^{-2}.

2.6. Computation methode

Density functional theory (DFT) calculations for periodic material systems were performed with the Vienna Ab initio simulation package (VASP) [19] using the projector-augmented wave (PAW) method [20]. The exchange–correlation function was handled using the generalized gradient approximation (GGA) formulated by the Perdew-Burke-Ernzerhof (PBE) [21]. The van der Waals (vdW) interactions were described with the DFT-D3 method in Grimme's scheme [22,23]. The interaction between the atomic core and electrons was described by the projector augmented wave method. The energy cutoff of plane-wave basis set was set to 500 eV [24]. The Brillouin zone was sampled with a 3 × 3 × 1 grid centered at the gamma (Γ) point for geometry relaxation. All the slabbed models possessed a vacuum distance of ≈15 Å to minimize the interlayer interactions [25]. The bottom layers about half of the structure were kept frozen at the lattice position. All structures with a dynamic magnetic moment were fully relaxed to optimize without any restriction until their total energies were converged to $<1 \times 10^{-6}$ eV, and the average residual forces were <0.02 eV/Å [26]. The solvent effects were considered by using the VASPSOL model [27]. Position-specific charge values were obtained using Bader analysis [28].

3. Results and discussion

3.1. The design principle of oxygen vacancy-rich TiO_2

TiO_2 nanoplates with different concentration of oxygen vacancy are successfully designed via a low-temperature annealing strategy. The phase structure of the synthesized MIL-125 (Ti) was confirmed by X-ray diffraction (XRD), which is assigned well to the simulated MIL-125 (Ti) pattern (Fig. S1a). The Fourier transform infrared (FT-IR) spectrum of the synthesized MIL-125 (Ti) shows characteristic vibrational bands for –COOH (1300–1800 cm^{-1}), benzene rings (700–1200 cm^{-1}), and O–Ti–O (400–800 cm^{-1}), further confirming the successful synthesis of the MIL-125 (Ti) (Fig. S1b) [18]. Additionally, scanning electron microscope (SEM) images reveal that MIL-125 (Ti) features a nanoplate morphology (Fig. S1c). To investigate the pyrolysis process of MIL-125 (Ti), the thermogravimetric analysis/derivative thermogravimetry (TG/DTG) of MIL-125 (Ti) was conducted in an air atmosphere. As shown in Fig. S2, the peak in the DTG curve at 450 °C suggests that the fastest pyrolysis rate and the most significant mass loss occurred at this temperature. The mass loss curve of MIL-125 (Ti) levels off beyond 460 °C, indicating the end of the pyrolysis process. During pyrolysis, increasing the heating rate leads to the rapid release of volatile gases (H_2O and CO_x), and it creates a local atmosphere with a low oxygen partial pressure that favors the formation of rich oxygen vacancies in TiO_2 [29]. Therefore, a low-temperature annealing strategy was used to prepare TiO_2 catalysts with different oxygen vacancy concentration by controlling the pyrolysis process of MIL-125 (Ti).

The microstructure of the TiO_2-400-10 and TiO_2-400-2 catalysts (Fig. S3a and S3b) maintains the nanoplate structure similar to that of the MIL-125 (Ti) precursor (Fig. S1c). The crystal structure of TiO_2 obtained from the pyrolysis of MIL-125 (Ti) precursors was analyzed using XRD. As shown in Fig. 2a, both the diffraction peaks of TiO_2-400-10 and TiO_2-400-2 are consistent with that of the anatase phase of TiO_2 (PDF#21-1272). Peaks at 25.28°, 36.95°, 37.80°, 38.58°, and 48.05° correspond to the (101), (103), (004), (112), and (200) crystal planes of anatase TiO_2, respectively. No additional diffraction peaks from MIL-125 (Ti) are observed, indicating the complete conversion of MIL-125

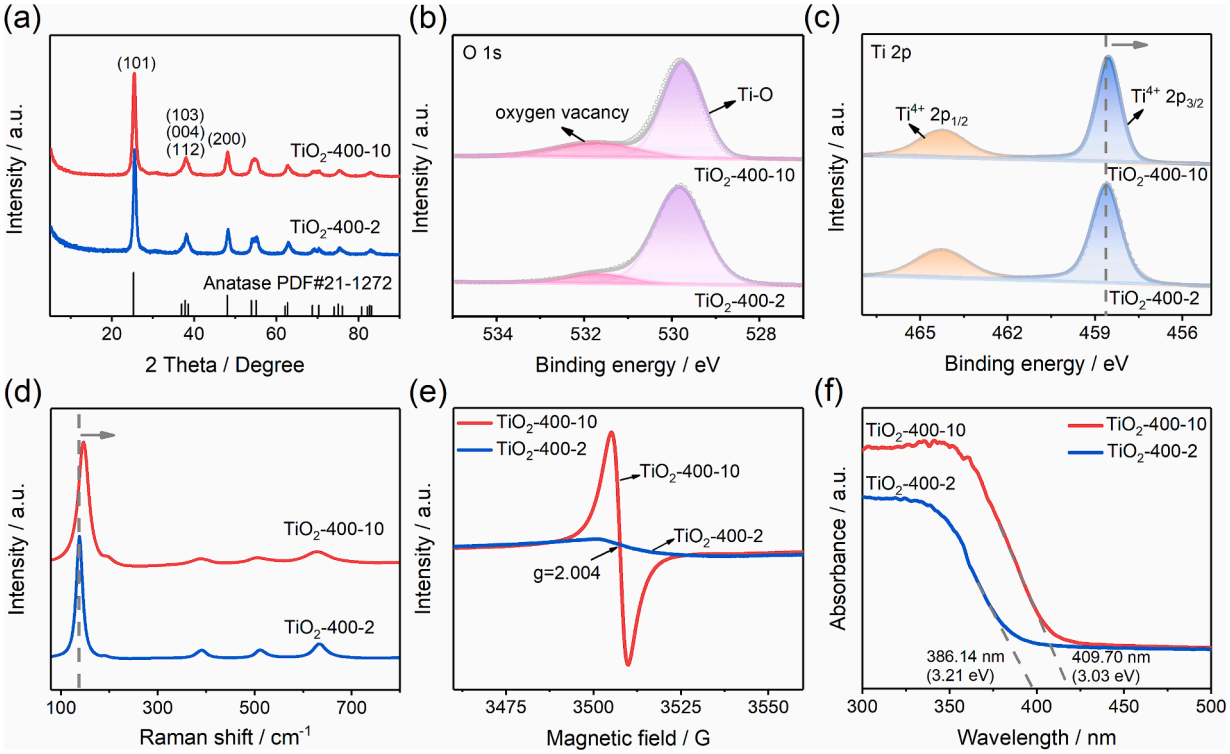

Fig. 2. (a) XRD patterns, (b) high-resolution O 1s XPS spectra, (c) high-resolution Ti 2p XPS spectra, (d) Raman spectra, (e) electron paramagnetic resonance spectra, and (f) UV–vis DRS spectra of TiO_2-400-10 and TiO_2-400-2.

(Ti) to TiO_2 during pyrolysis. The specific surface area and pore size distribution of TiO_2-400-10 and TiO_2-400-2 were analyzed using N_2 adsorption–desorption isotherms and the BJH method. As shown in Fig. S4, the BET surface area of the TiO_2-400-2 catalyst is 78.10 $m^2\ g^{-1}$, while that of the TiO_2-400-10 catalyst is 98.25 $m^2\ g^{-1}$. Both samples exhibit similar specific surface areas and pore size distributions.

The existence and concentration of oxygen vacancies in TiO_2 were evaluated by X-ray photoelectron spectroscopy (XPS), Raman spectrum, Electron paramagnetic resonance (EPR), and TG. The high-resolution O 1s XPS spectra of TiO_2 can be deconvoluted into two peaks (Fig. 2b), corresponding to lattice oxygen in Ti–O ($O_{lattice}$, 529.83 eV) and chemical-absorbed oxygen species at oxygen vacancies ($O_{vacancy}$, 531.65 eV), respectively [30,31]. Based on the deconvoluted O 1s XPS, the ratio of oxygen vacancies in TiO_2 can be estimated as ($O_{vacancy}$ area)/($O_{vacancy}$ area + $O_{lattice}$ area) [32]. The larger ratio of oxygen vacancies in TiO_2-400-10 suggests a higher concentration of oxygen vacancies in TiO_2-400-10. Moreover, the high-resolution Ti 2p XPS spectra (Fig. 2c) show that the binding energy of Ti $2p_{3/2}$ in TiO_2-400-10 shifts to a lower value compared to TiO_2-400-2, suggesting the increased electron density around Ti atoms due to adjacent positively charged oxygen vacancies [33–35]. The XPS spectra confirm that oxygen vacancy-rich TiO_2 was successfully synthesized. The positively charged oxygen vacancies are promising to act as the electron collector to enhance the reaction kinetics of the rate-determining step of V^{2+}/V^{3+}.

The crystal structure and oxygen vacancy concentration of the catalyst are also confirmed by Raman spectra. In Fig. 2d, the four peaks of TiO_2-400 at 138, 391, 511, and 633 cm^{-1} can be assigned as the E_g, B_{1g}, A_{1g}, and E_g vibrational modes of anatase TiO_2, respectively, consistent with the XRD result [36]. Additionally, Raman spectra of TiO_2-400-10 show a noticeable blue shift of the E_g vibrational peak and broader half-peak widths than TiO_2-400-2. The blue shift of Raman peak likely results from the reduced symmetry of the Ti-O bonds, while the broadening and weakening of the Raman peaks typically indicate increasing structure defects [36,37]. Therefore, the changes in Raman spectra of TiO_2-400-10 can be attributed to the abundant oxygen vacancy. The oxygen vacancy concentration in the catalysts is further investigated by EPR spectra. EPR signals at g = 2.002 correspond to unpaired electrons trapped by the oxygen vacancies [38]. As shown in Fig. 2e, compared to TiO_2-400-2, TiO_2-400-10 exhibits a significant EPR signal at around g = 2.002, indicating a higher oxygen vacancy concentration in TiO_2-400-10 [39]. The concentration of oxygen vacancy is also characterized by TG [38,40]. On the basis of TG results (Fig. S5 and S6), the chemical formula of oxygen vacancy-rich TiO_2-400-10 and oxygen vacancy-deficient TiO_2-400-2 are estimated to be $TiO_{1.93}$ and $TiO_{1.95}$, respectively. The delocalized electrons generated by oxygen vacancies can increase the density of states near the Fermi level, enhancing the conductivity of TiO_2 [41]. UV–vis DRS is used to further demonstrate that the increased oxygen vacancies can efficiently improve the intrinsic conductivity of TiO_2. As shown in Fig. 2f, oxygen vacancy-deficient TiO_2-400-2 exhibits a typical UV–vis absorption spectra of anatase TiO_2 with an absorption edge wavelength of 386.14 nm, corresponding to a bandgap of 3.21 eV, while the absorption edge of the oxygen vacancy-rich TiO_2-400-10 shows an evident red shift to 409.70 nm, with a reduced bandgap of 3.03 eV [35]. The band gap of TiO_2 is calculated by the formula $E_g = 1240/\lambda$. The reduced bandgap of oxygen vacancy-rich TiO_2-400-10 indicates that the higher concentration of oxygen vacancies effectively enhances the intrinsic conductivity of TiO_2, facilitating the charge transfer process of V^{2+}/V^{3+}.

To evaluate the impact of oxygen vacancy concentration on the redox kinetics of V^{2+}/V^{3+}, a typical three-electrode system was used to assess the electrochemical properties of TiO_2-400-10 and TiO_2-400-2 [42]. As shown in Fig. 3a, TiO_2-400-10 exhibits a higher oxidation current density and a more negative oxidation peak potential compared with TiO_2-400-2. The results indicate that oxygen vacancies can effectively reduce the reaction overpotential of the electrochemical oxidation of V^{2+} [43]. EIS was employed to evaluate the impact of oxygen vacancy concentration on the electron transfer process of V^{2+}/V^{3+} (Fig. 3b) [44]. TiO_2-400-10 shows a smaller charge transfer resistance than TiO_2-400-2. The specific charge transfer resistance obtained from equivalent circuit fitting is shown in Table S1. Similar results are also observed when

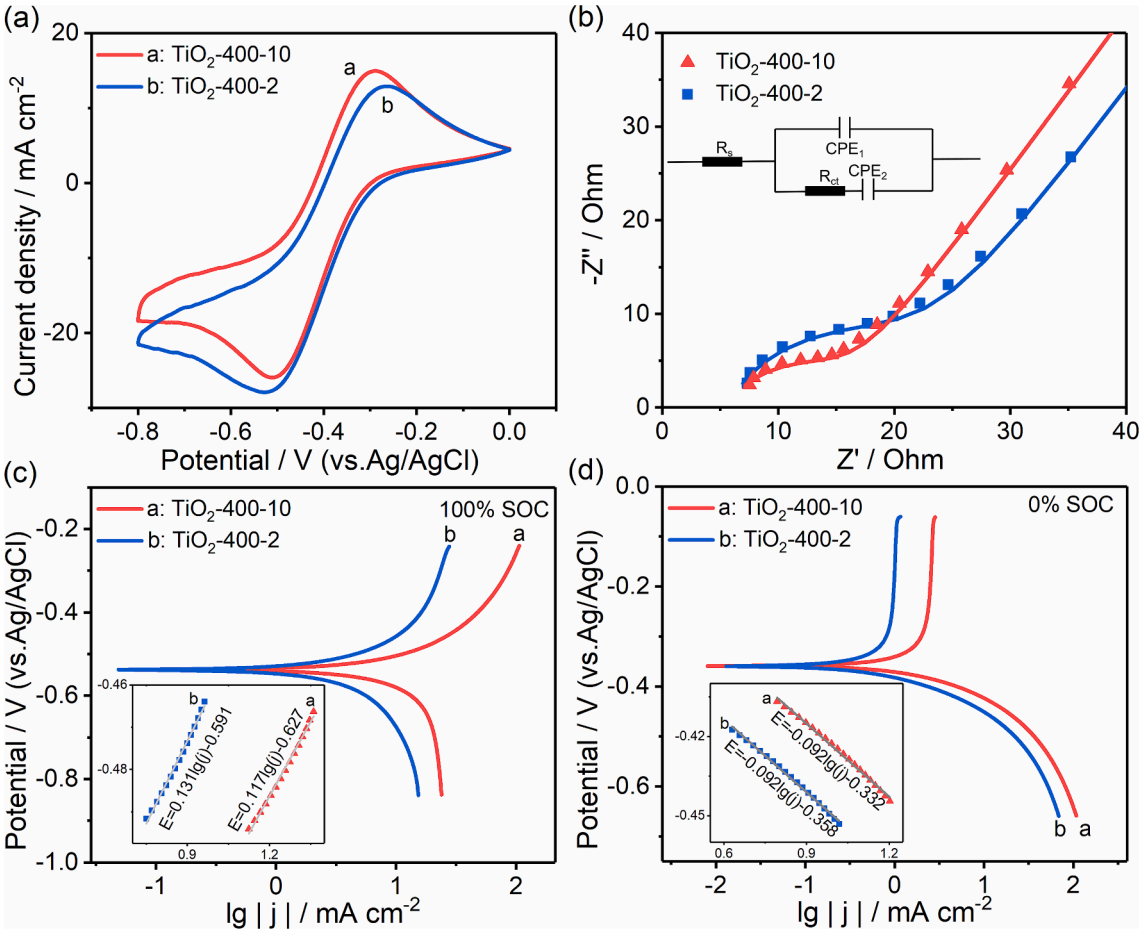

Fig. 3. (a) CV curves at a scan rate of 10 mV s^{-1}, and (b) Nyquist plots of TiO_2-400-10 and TiO_2-400-2 in 1.8 M V^{3+} + 3.6 M H_2SO_4 electrolyte. Tafel plots of TiO_2-400-10 and TiO_2-400-2 at (c) 100 %, (d) 0 % SOC in 1.8 M vanadium + 3.6 M H_2SO_4.

oxygen vacancy-rich TiO_2-400-10 and oxygen vacancy-deficient TiO_2-400-2 loaded on GF (Fig. S7). These results demonstrate that oxygen vacancy-rich TiO_2-400-10 can accelerate the electron transfer kinetics of V^{2+}/V^{3+}. Tafel plots at different state of charge (SOC) were further measured to assess the catalytic effect of oxygen vacancies on the reaction kinetics of V^{2+}/V^{3+} [45]. Compared to oxygen vacancy-deficient TiO_2-400-2, the exchange current density of oxygen vacancy-rich TiO_2-400-10 at 100 % SOC increases from 2.57 × 10^{-3} A cm^{-2} to 5.84 × 10^{-3} A cm^{-2} in the oxidation process, an increase of 127.24 % (Fig. 3c). While the exchange current density at 0 % SOC only increases by 91.26 % (from 1.03 × 10^{-3} A cm^{-2} to 1.97 × 10^{-3} A cm^{-2}) in the reduction process (Fig. 3d). Tafel plots of oxygen vacancy-rich TiO_2-400-10 and oxygen vacancy-deficient TiO_2-400-2 at 50 % SOC were also tested shown in Fig. S8. This demonstrates that oxygen vacancy-rich TiO_2-400-10 can significantly enhance the reaction kinetics of V^{2+}/V^{3+}, particularly for the electrochemical oxidation of V^{2+}, which is the rate-determining step of V^{2+}/V^{3+}. Furthermore, the electrochemical active surface area (ECSA) of the catalysts was evaluated by calculating the double-layer capacitance (Fig. S9) [46]. Oxygen vacancy-rich TiO_2-400-10 and oxygen vacancy-deficient TiO_2-400-2 possess similar double-layer capacitance and comparable ECSA, indicating that the superior catalytic activity of TiO_2-400-10 originates from its intrinsic catalytic activity of oxygen vacancies.

Meanwhile, the impact of pyrolysis temperature on the oxygen vacancy concentration of the catalyst was probed. In Fig. S10, when the pyrolysis temperature is lowered to 350 °C, XRD diffraction peaks of the pyrolysis product exhibit both the characteristic peaks of the precursor MIL-125 (Ti) and anatase TiO_2, implying the incomplete pyrolysis of MIL-125 (Ti). As the pyrolysis temperature increases from 400 °C to 500 °C or 600 °C, the relative intensity of peaks of rutile TiO_2 gradually increases due to the higher thermal stability of rutile TiO_2 (Fig. 4a). In addition, the sharper diffraction peaks at higher pyrolysis temperature indicate the improved crystallinity and reduced oxygen vacancy concentration of the synthesized TiO_2 catalyst. SEM images display that TiO_2 obtained at different temperature maintains the nanoplate morphology (Fig. S11). As exhibited in Fig. 4b, elevating the pyrolysis temperature of the precursor results in a significant decrease in the specific surface area of TiO_2. The BET surface area of the TiO_2-400-10 catalyst is 98.25 m^2/g, while it decreases to 27.96 m^2/g and 11.10 m^2/g for TiO_2-500-10 and TiO_2-600-10, respectively. A lower specific surface area hinders the exposure of active sites, reducing the catalytic activity of the catalyst. XPS and EPR further characterize the oxygen vacancy concentration in TiO_2-400-10, TiO_2-500-10, and TiO_2-600-10 synthesized at various temperature. In comparison to TiO_2-500-10 and TiO_2-600-10, TiO_2-400-10 exhibits the highest ratio of oxygen vacancies and the lowest binding energy of Ti $2p_{3/2}$, indicating a significant decrease of oxygen vacancies at higher temperature (Fig. 4d and e). Besides, the peak intensity at g = 2.002 in EPR considerably decreases as the pyrolysis temperature increases, implying the highest oxygen vacancy concentration in TiO_2-400-10 (Fig. 4c).

As mentioned previously, CV, EIS, and Tafel plots reveal a strong correlation between the concentration of oxygen vacancy and the catalytic activity toward V^{2+}/V^{3+}. As the pyrolysis temperature increases, the oxygen vacancy concentration of TiO_2 decreases, resulting in a decline in its catalytic activity. In CV curves (Fig. 4f), oxygen vacancy-rich TiO_2-400-10 demonstrates the smallest separation of peak

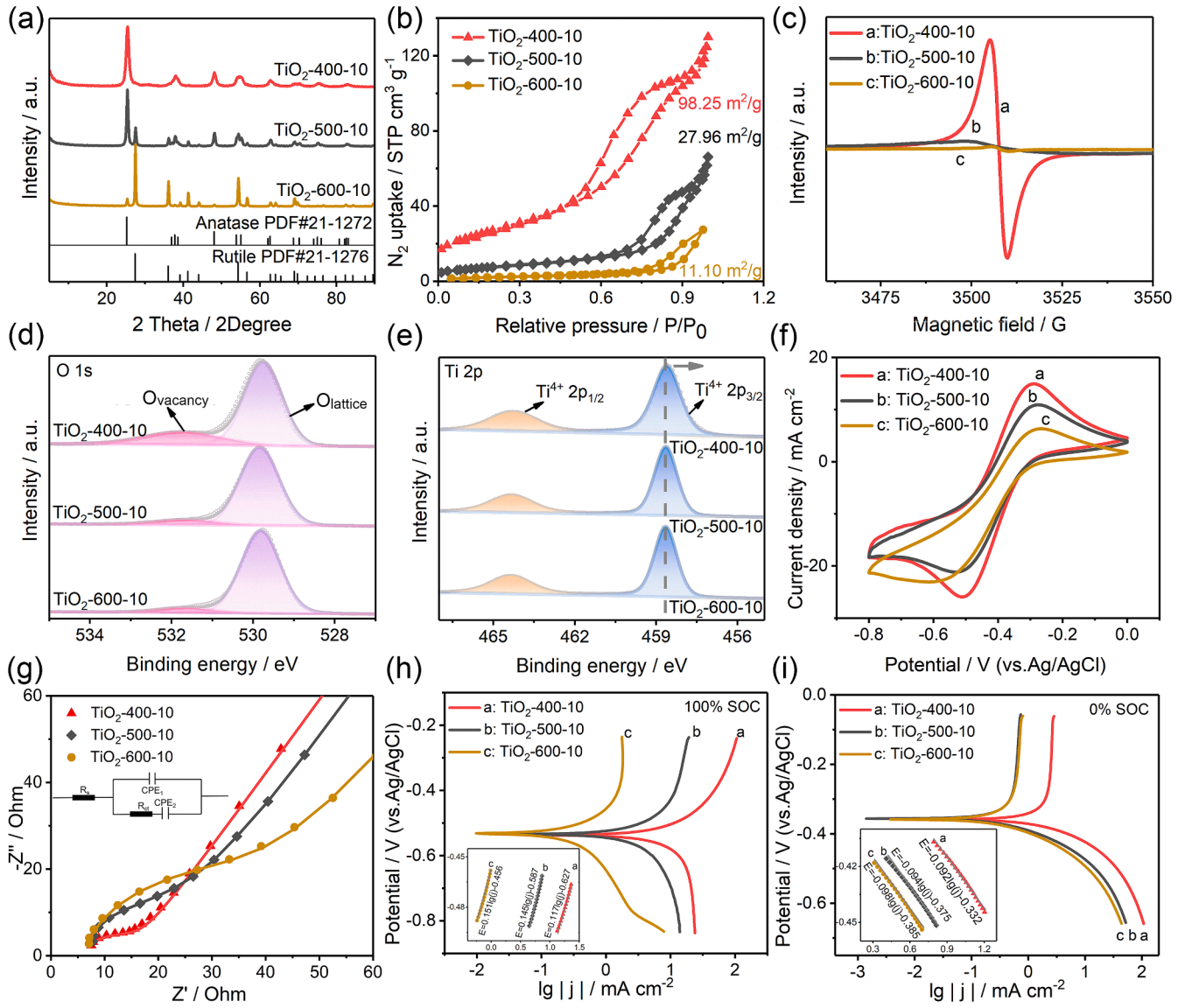

Fig. 4. (a) XRD patterns, (b) nitrogen adsorption–desorption isotherms, (c) electron paramagnetic resonance spectra, (d) high-resolution O 1s XPS spectra, and (e) high-resolution Ti 2p XPS spectra of TiO_2-400-10, TiO_2-500-10, and TiO_2-600-10. (f) CV curves at a scan rate of 10 mV s^{-1} and (g) Nyquist plots of TiO_2-400-10, TiO_2-500-10, and TiO_2-600-10 in 1.8 M V^{3+} + 3.6 M H_2SO_4 electrolyte. Tafel plots of TiO_2-400-10, TiO_2-500-10, and TiO_2-600-10 at (h) 100 %, (i) 0 % SOC in 1.8 M vanadium + 3.6 M H_2SO_4.

potential and the highest redox current density among these catalysts. The LSV curves (Fig. S12) further reveal that oxygen vacancy-rich TiO_2-400-10 exhibits the lowest reaction overpotential and the highest reaction current. These results indicate that oxygen vacancy-rich TiO_2-400-10 can significantly enhance the reversibility and reactivity of V^{2+}/V^{3+} [47]. EIS results indicate that oxygen vacancy-rich TiO_2-400-10 significantly accelerates the electron transfer process of V^{2+}/V^{3+} (Fig. 4g) [48]. The specific charge transfer resistance (Rct) obtained from equivalent circuit fitting is shown in Table S2. In Fig. 4h and i, oxygen vacancy-rich TiO_2-400-10 can proficiently promote the reaction kinetics of the electrochemical oxidation of V^{2+}. The exchange current density of the electrochemical oxidation of V^{2+} increases by a factor of 17.48, from 3.16 × 10^{-4} A cm^{-2} to 5.84 × 10^{-3} A cm^{-2} (Fig. 4h). In contrast, the exchange current density in the electrochemical reduction process enlarges only by a factor of 2.88, from 5.08 × 10^{-4} A cm^{-2} to 1.97 × 10^{-3} A cm^{-2} (Fig. 4i). These results demonstrate that oxygen vacancy-rich TiO_2-400-10 can specifically boost the reaction kinetics of the electrochemical oxidation of V^{2+}.

3.2. *Theoretical modeling of the activity origin of oxygen vacancy*

To further clarify the origin of the catalytic activity of oxygen vacancy in TiO_2, density functional theory (DFT) calculations were carried out to elucidate how the oxygen vacancy concentration affects the reaction kinetics of V^{2+}/V^{3+}. TiO_2 models with one and two oxygen vacancies were used as oxygen vacancy-deficient and oxygen vacancy-rich models, respectively [39]. The theoretical calculation models for the three catalysts TiO_2, oxygen vacancy-poor TiO_2, and oxygen vacancy-rich TiO_2 are shown in Fig. S13, 5a, and b. First, the band gap is calculated to investigate the impact of oxygen vacancy concentration on the structure property of the TiO_2 because the band gap plays a crucial role in determining the electron transfer process during the catalytic reaction [49]. The calculated band gap of oxygen vacancy-rich TiO_2 is 2.05 eV, while that of oxygen vacancy-deficient TiO_2 is 2.23 eV (Fig. 5c and d). Theoretical calculation indicates that the introduction of oxygen vacancies can remarkably reduce the band gap of TiO_2, facilitating the electron transfer process of V^{2+}/V^{3+}. The effect of oxygen vacancies on the band gap of TiO_2 exhibits a consistent trend between the DFT results

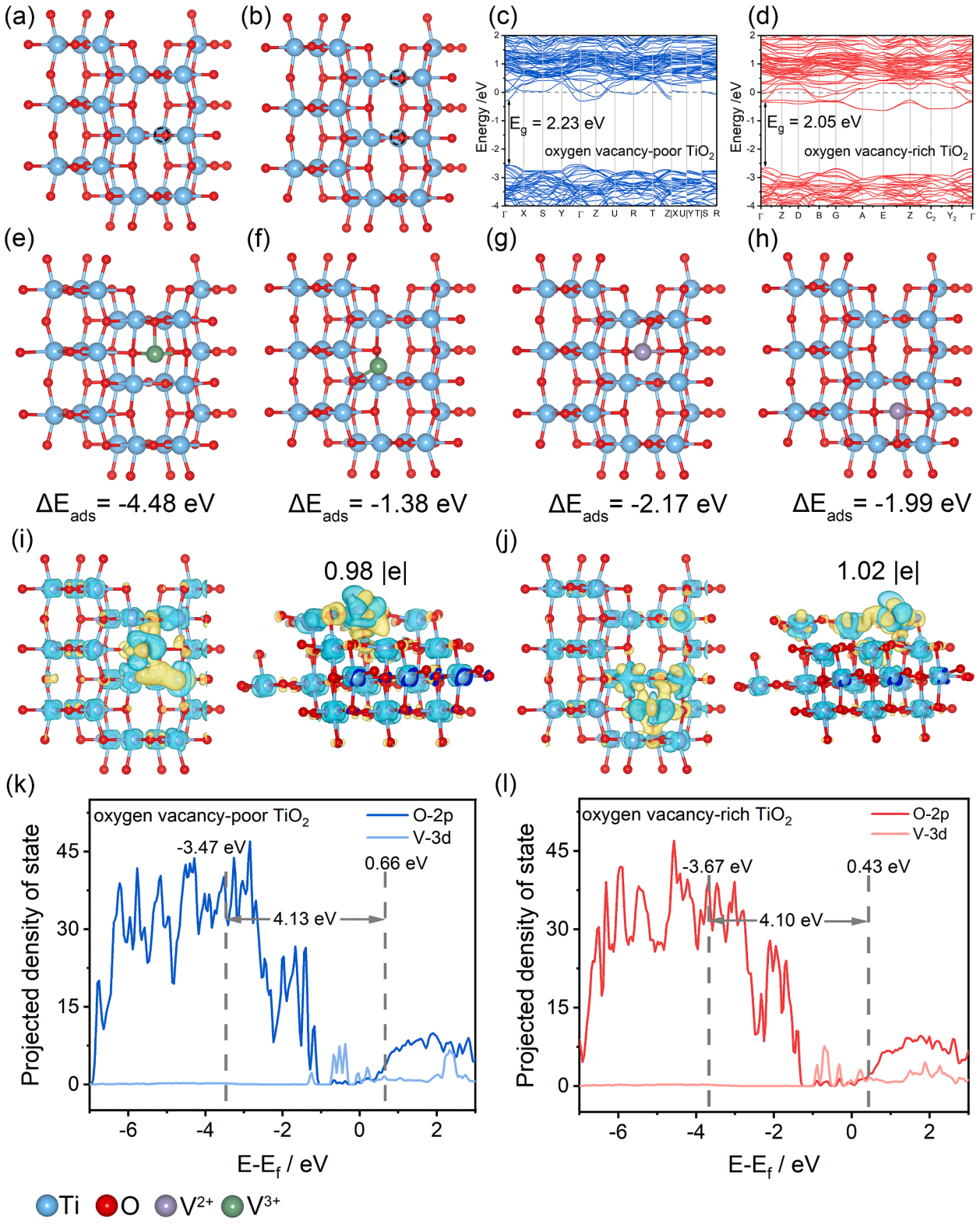

Fig. 5. DFT-calculated structural models of (a) oxygen-vacancy poor TiO_2 and (b) oxygen-vacancy rich TiO_2, where the black dashed balls represent oxygen vacancies. Calculated band structure of (c) oxygen-vacancy poor TiO_2 and (d) oxygen-vacancy rich TiO_2. Comparison of adsorption energy of V^{3+} on (e) oxygen-vacancy poor TiO_2 and (f) oxygen-vacancy rich TiO_2. Comparison of adsorption energy of V^{2+} on (g) oxygen-vacancy poor TiO_2 and (h) oxygen-vacancy rich TiO_2. Electron density difference diagrams of (i) oxygen-vacancy poor TiO_2 and (j) oxygen-vacancy rich TiO_2 with adsorbed V^{2+} under different viewing angles. Projected density of states of V 3d and O 2p orbitals in (k) oxygen-vacancy poor TiO_2 and (l) oxygen-vacancy rich TiO_2. Blue, red, purple, and green spheres represent Ti, O, V^{2+}, and V^{3+}, respectively. Yellow indicates electron accumulation, and cyan denotes electron deletion in electron density difference diagrams. (For interpretation of the references to colour in this figure legend, the reader is referred to the web version of this article.)

and UV–vis absorption spectra. The underestimated band gap in DFT can be ascribed to delocalization errors caused by incomplete removal of Coulomb self-interaction [50].

The impact of oxygen vacancy concentration on the catalytic mechanism was further revealed by DFT calculations. The fundamental catalytic process for the catalysts towards V^{2+}/V^{3+} involves three basic steps, adsorption, electron transfer, and desorption [51]. The adsorption energy of V^{2+} and V^{3+} on both oxygen vacancy-deficient and oxygen vacancy-rich TiO_2 were calculated. The adsorption energy of V^{3+} on oxygen vacancy-rich TiO_2 (−1.38 eV) is more positive than that on oxygen vacancy-deficient TiO_2 (−4.48 eV), indicating that a higher oxygen vacancy concentration can promote the desorption of V^{3+} (Fig. 5e and f). The accelerated desorption process of V^{3+} on oxygen vacancy-rich TiO_2 can be attributed to the positively charged oxygen vacancy. The adsorption energy of V^{2+} on oxygen vacancy-rich TiO_2 (−1.99 eV) and oxygen vacancy-deficient TiO_2 (−2.17 eV) show that both models favor V^{2+} adsorption (Fig. 5g and h). These results suggest that during the electrochemical oxidation of V^{2+}, a higher oxygen vacancy concentration effectively facilitates the desorption process of V^{3+}, thereby accelerating the reaction kinetics of V^{2+}/V^{3+}. The microelectronic interaction between vanadium ions and TiO_2 with different oxygen vacancy concentration was further revealed through electron density difference. Based on Bader charge analysis (Fig. 5i and j), V^{2+} on oxygen vacancy-rich TiO_2 lost more electrons (1.02|e|) than oxygen vacancy-deficient TiO_2 (0.98|e|), indicating that a higher oxygen vacancy concentration can promote the electrochemical oxidation of V^{2+} to V^{3+}, thereby enhancing the electron transfer process of V^{2+}/V^{3+}. The projected density of states (PDOS) of the V 3d and O 2p bands were also calculated for V^{2+} on the surface of TiO_2 with different concentration of oxygen vacancies (Fig. 5k and l). The results imply that oxygen vacancy-rich TiO_2 (4.10 eV) exhibits a smaller d-p band center gap for V^{2+} than oxygen vacancy-poor TiO_2 (4.13 eV). A smaller d-p band center gap corresponds to a more pronounced d-p hybridization between the V 3d and O 2p orbitals, thereby greatly facilitating the electron transfer of V^{2+}/V^{3+}. In conclusion, DFT calculations reveal that a high oxygen vacancy concentration in TiO_2 effectively facilitates the electrochemical oxidation of V^{2+}, which is the rate-determining step of V^{2+}/V^{3+}.

3.3. VRFB performance

To further probe the impact of oxygen vacancy concentration on the reaction kinetics of V^{2+}/V^{3+} during battery operation, VRFB were assembled using oxygen vacancy-rich TiO_2 loaded GF (TiO_2-400-10), oxygen vacancy-deficient TiO_2 loaded GF (TiO_2-400-2), and unmodified GF (GF) as negative electrode, respectively (Fig. 6a). TiO_2-400-10 and TiO_2-400-2, which have similar key physicochemical properties but

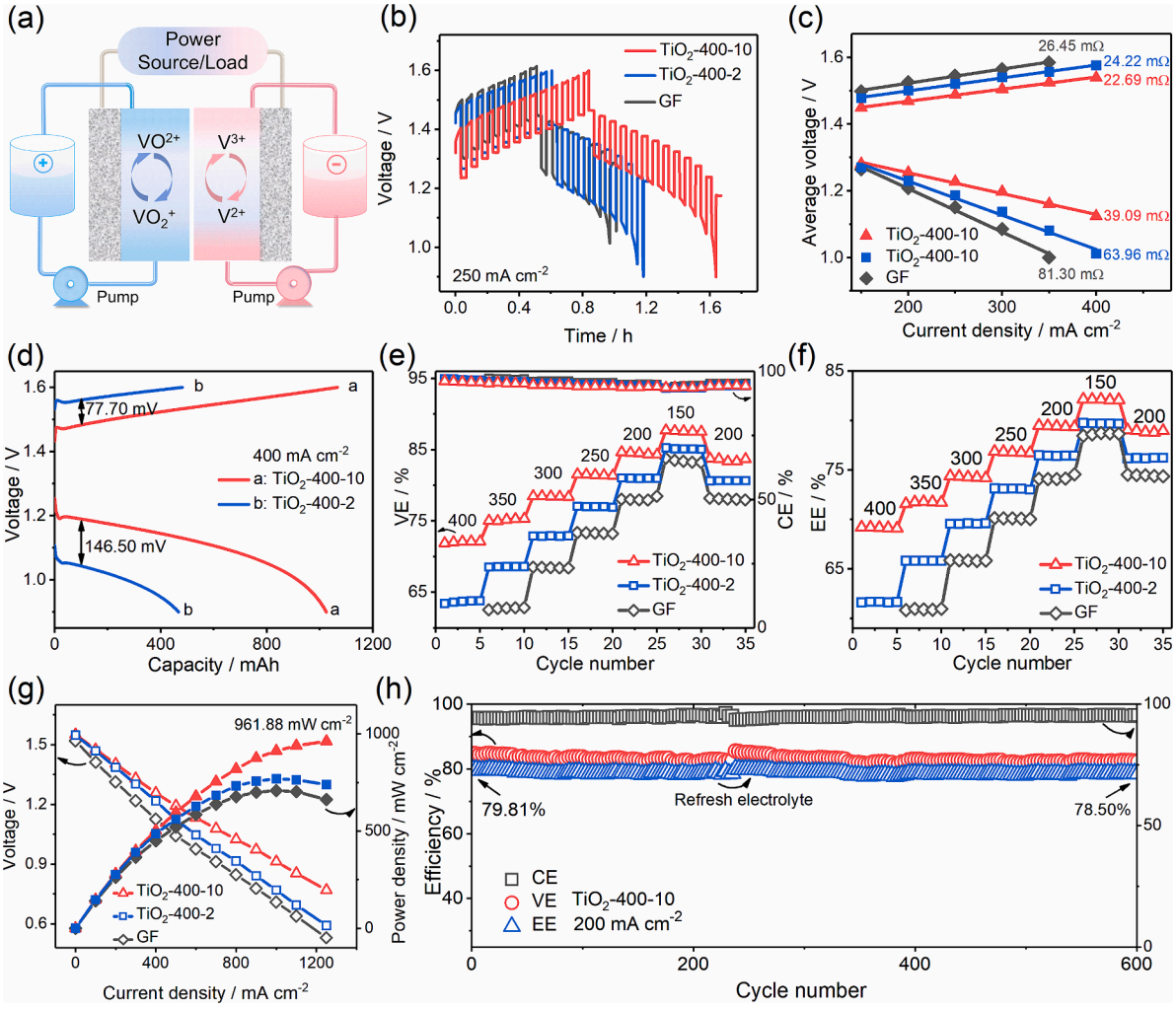

Fig. 6. (a) Illustration of the VRFB with different oxygen vacancy concentration TiO_2. (b) GITT curves, (c) average charge and discharge voltages, (d) charge–discharge curves, (e) voltage efficiency and coulombic efficiency, and (f) energy efficiency of VRFB with TiO_2-400-10, TiO_2-400-2, and GF electrode at varied current densities. (g) Polarization curves and corresponding power density plots of VRFB with TiO_2-400-10, TiO_2-400-2, and GF electrode at 0 % SOC. (h) Energy efficiencies of VRFB with TiO_2-400-10 electrode during long-term stability test at 200 mA cm^{-2}.

different oxygen vacancy concentration, were selected for investigation. Galvanostatic intermittent titration technique (GITT) was applied to analyze the effect of oxygen vacancy concentration on the battery overpotential. As shown in Fig. 6b, the battery modified with oxygen vacancy-rich TiO_2-400-10 exhibits a significantly lower overpotential and a higher electrolyte utilization in comparison with oxygen vacancy-deficient TiO_2-400-2 and GF. Furthermore, according to the calculated battery resistance (Fig. 6c), compared to oxygen vacancy-deficient TiO_2-400-2 (63.96 mΩ), the battery modified with oxygen vacancy-rich TiO_2-400-10 (39.09 mΩ) can effectively lower the battery resistance, especially for the discharge process. Considering that only the negative electrode is modified with different oxygen vacancy concentration in VRFB, while other components remain consistent, the differences in battery performance can be ascribed to the changes in the V^{2+}/V^{3+} redox kinetics. Thus the oxygen vacancy-rich TiO_2-400-10 promotes the redox kinetics of the electrochemical oxidation of V^{2+} by enhancing its desorption and electron transfer process, which is consistent with the aforementioned results of the electrochemical performance test. The charge–discharge curves of the battery (Fig. 6d) also reveal that a high oxygen vacancy concentration in TiO_2 can significantly lower the overpotential of the electrochemical oxidation of V^{2+}. Moreover, owing to the enhanced redox kinetics of the electrochemical oxidation of V^{2+}, the battery with a high concentration of oxygen vacancy TiO_2 exhibits a higher discharge capacity, indicating the improved electrolyte utilization, which is essential for reducing the high electrolyte cost in VRFB (Fig. 6d).

The considerably reduced overpotential endows the battery with excellent rate performance, particularly at the high current density [52]. As depicted in Fig. 6e, the battery with oxygen vacancy-rich TiO_2-400-10 demonstrates a superior voltage efficiency (VE) over oxygen vacancy-deficient TiO_2 within the current density range of 150–400 mA cm^{-2}. Given the same Nafion 212 membrane used in the batteries, the batteries assembled with TiO_2 featuring different oxygen vacancy concentration display comparable Coulombic efficiency (CE). As energy efficiency (EE) is determined by the VE and CE, the EE of the battery demonstrates a similar trend to VE (Fig. 6f). As the current density increases, both VE and EE of the battery decrease, resulting from the elevated battery polarization. Contributing to the high catalytic activity of oxygen vacancies, the EE of the battery modified with oxygen vacancy-rich TiO_2-400-10 is superior to that of the batteries modified with oxygen vacancy-deficient TiO_2-400-2 and GF. At 300 mA cm^{-2}, the EE of oxygen vacancy-rich TiO_2-400-10 is 74.39 %, which is 4.81 % higher than that of oxygen vacancy-deficient TiO_2-400-2 and 8.58 % higher than that of GF. The excellent rate performance of oxygen vacancy-rich TiO_2-400-10 indicates that improving the redox kinetics of the electrochemical oxidation of V^{2+} can significantly improve the battery performance. In Fig. 6g, polarization curves also confirm that oxygen vacancy-rich TiO_2-400-10 effectively reduces the battery overpotential, especially at the high current density. More importantly, the battery assembled with oxygen vacancy-rich TiO_2-400-10 reaches a remarkable power density of 961.88 mW cm^{-2}, while that of oxygen vacancy-deficient TiO_2-400-2 is 768.90 mW cm^{-2}, and that of GF is 708.60 mW cm^{-2}. The significantly enhanced power density is crucial for reducing the stack size, ultimately lowering the cost of VRFB, which is conducive to the commercial application [53]. To further evaluate the stability of catalysts, the long-term cycling performance was carried out (Fig. 6h). Oxygen vacancy-rich TiO_2-400-10 achieves 79.81 % energy efficiency at 200 mA cm^{-2} and demonstrates outstanding cycling stability over 600 charge–discharge cycles with an EE decay rate of only 0.0022 % per cycle. Therefore, these results not only reveal a strong correlation between the oxygen vacancy concentration and the catalytic activity toward V^{2+}/V^{3+}, but also confirm that oxygen vacancies can significantly enhance the battery performance by accelerating the redox kinetics of the electrochemical oxidation of V^{2+} to V^{3+}.

4. Conclusion

In summary, the structure–activity relationship between the oxygen vacancy and redox kinetics of V^{2+}/V^{3+} is revealed. The high catalytic activity of oxygen vacancy-rich TiO_2 is attributed to the redistribution of the electronic structure caused by the oxygen vacancies which act as electron acceptors, thus accelerating the desorption and electron transfer processes in the electrochemical oxidation process of V^{2+}. Oxygen vacancy-rich TiO_2 significantly boosts the sluggish redox kinetics of V^{2+}/V^{3+} by accelerating the electrochemical oxidation of V^{2+} to V^{3+}, compared to oxygen vacancy-deficient TiO_2. The battery modified with oxygen vacancy-rich TiO_2 exhibits outstanding battery performance ranging from 150 to 400 mA cm^{-2}, achieving an energy efficiency of 74.39 % at 300 mA cm^{-2} and a high power density of 961.88 mW cm^{-2}. Moreover, the battery modified with oxygen vacancy-rich TiO_2 exhibits excellent stability with an average decay rate of only 0.0022 % per cycle for 600 cycles. This study offers insights into the regulation of oxygen vacancy concentration in metal oxides and sheds light on the development of highly active catalysts for VRFBs.

CRediT authorship contribution statement

Rongjiao Huang: Writing – review & editing, Writing – original draft, Visualization, Data curation, Conceptualization. **Shuhao Su:** Visualization, Validation. **Yincheng Wang:** Visualization, Validation. **Suqin Liu:** Writing – review & editing, Supervision, Resources, Project administration, Funding acquisition. **Zhen He:** Writing – review & editing, Supervision. **Li Tian:** Writing – review & editing. **Dong Luo:** Writing – review & editing. **Haikun Xu:** Software, Resources. **Jue Wang:** Writing – review & editing, Writing – original draft, Supervision, Project administration, Funding acquisition.

Declaration of competing interest

The authors declare that they have no known competing financial interests or personal relationships that could have appeared to influence the work reported in this paper.

Acknowledgment

This work was financially supported by the National Natural Science Foundation of China (Grant Nos. 51972345), the Natural Science Foundation of Changsha City (Grant Nos. kq2402205), the Hunan Province Science and Technology Innovation Plan Project (Grant Nos. 2024QY2013), and the Hunan Province College Students' Innovation and Entrepreneurship Training Program Project (Grant Nos. S2024105340097).

Appendix A. Supplementary data

Supplementary data to this article can be found online at https://doi.org/10.1016/j.jcis.2025.137281.

Data availability

Data will be made available on request.

References

[1] J. Lei, Y. Zhang, Y. Yao, Y. Shi, K.L. Leung, J. Fan, Y. Lu, An active and durable molecular catalyst for aqueous polysulfide-based redox flow batteries, Nat. Energy 8 (2023) 1355–1364, https://doi.org/10.1038/s41560-023-01370-0.
[2] Z. Wei, Z. Huang, G. Liang, Y. Wang, S. Wang, Y. Yang, T. Hu, C. Zhi, Starch-mediated colloidal chemistry for highly reversible zinc-based polyiodide redox flow batteries, Nat. Commun. 15 (2024) 3841, https://doi.org/10.1038/s41467-024-48263-8.
[3] H. Zhang, W. Xu, W. Song, K. Peng, L. Sun, C. Yang, X. Zhang, H. Zhang, B. Ye, X. Liang, High-performance spiro-branched polymeric membranes for

sustainability applications, Nat. Sustain., 7 (2024) 1–10, https://doi.org/10.1038/s41893-024-01364-0.
[4] F. Xing, Q. Fu, F. Xing, J. Zhao, H. Long, T. Liu, X. Li, Bismuth single atoms regulated graphite felt electrode boosting high power pensity vanadium flow batteries, J. Am. Chem. Soc. 146 (2024) 26024–26033, https://doi.org/10.1021/jacs.4c04951.
[5] L. Ye, S. Qi, T. Cheng, Y. Jiang, Z. Feng, M. Wang, Y. Liu, L. Dai, L. Wang, Z. He, Vanadium redox flow battery: review and perspective of 3D electrodes, ACS Nano 18 (2024) 18852–18869, https://doi.org/10.1021/acsnano.4c06675.
[6] X. Huangyang, H. Wang, W. Zhou, Q. Deng, Z. Liu, X.-X. Zeng, X. Wu, W. Ling, In situ growth of amorphous MnO_2 on graphite felt via mild etching engineering as a powerful catalyst for advanced vanadium redox flow batteries, ACS Appl. Mater. Interfaces 16 (2024) 32189–32197, https://doi.org/10.1021/acsami.4c02971.s001.
[7] F. Zhu, W. Guo, Y. Fu, Functional materials for aqueous redox flow batteries: merits and applications, Chem. Soc. Rev. 52 (2023) 8410–8446, https://doi.org/10.1039/d3cs00703k.
[8] F. Huang, X. Chen, H. Sun, Q. Zeng, J. Ma, D. Wei, J. Zhu, Z. Chen, T. Liang, X. Yin, Atmosphere induces tunable oxygen vacancies to stabilize single-atom copper in ceria for robust electrocatalytic CO_2 reduction to CH_4, Angew. Chem. Int. Ed. 64 (2024), https://doi.org/10.1002/anie.202415642 e202415642.
[9] J. Qu, W. Liu, R. Liu, J. He, D. Liu, Z. Feng, Z. Feng, R. Li, C. Li, Evolution of oxygen vacancies in cerium dioxide at atomic scale under CO_2 reduction, Chem Catal. 3 (2023) 100759, https://doi.org/10.1016/j.checat.2023.100759.
[10] J. Vázquez-Galván, C. Flox, C. Fàbrega, E. Ventosa, A. Parra, T. Andreu, J. R. Morante, Hydrogen-treated rutile TiO_2 shell in graphite-core structure as a negative electrode for high-performance vanadium redox flow batteries, ChemSusChem 10 (2017) 2089–2098, https://doi.org/10.1002/cssc.201700017.
[11] A.W. Bayeh, D.M. Kabtamu, Y.C. Chang, G.C. Chen, H.Y. Chen, T.R. Liu, T. H. Wondimu, K.C. Wang, C.H. Wang, Hydrogen-treated defect-rich $W_{18}O_{49}$ nanowire-modified graphite felt as high-performance electrode for vanadium redox flow battery, ACS Appl. Energy Mater. 2 (2019) 2541–2551, https://doi.org/10.1021/acsaem.8b02158.
[12] R.C. Zhang, K. Li, S.Z. Ren, J.F. Chen, X.J. Feng, Y.Q. Jiang, Z.X. He, L. Dai, L. Wang, Sb-doped SnO_2 nanoparticle-modified carbon paper as a superior electrode for a vanadium redox flow battery, Appl. Surf. Sci. 526 (2020) 146685, https://doi.org/10.1016/j.apsusc.2020.146685.
[13] A.W. Bayeh, G.Y. Lin, Y.C. Chang, D.M. Kabtamu, G.C. Chen, H.Y. Chen, K. C. Wang, Y.M. Wang, T.C. Chiang, H.C. Huang, C.H. Wang, Oxygen-vacancy-rich cubic CeO_2 nanowires as catalysts for vanadium redox flow batteries, ACS Sustain. Chem. Eng. 8 (2020) 16757–16765, https://doi.org/10.1021/acssuschemeng.0c03861.
[14] J. Choi, J. Park, J. Park, M. Kim, S. Lee, C.R. Cho, J.H. Lee, Y. Park, M.G. Kim, J. Choi, J.-W. Park, M. Park, Low-index facet polyhedron-shaped binary cerium titanium oxide for high-voltage aqueous zinc–vanadium redox flow batteries, ACS Appl. Mater. Interfaces 15 (2023) 55692–55702, https://doi.org/10.1021/acsami.3c11734.
[15] Y. Jiang, Z. Liu, Y. Lv, A. Tang, L. Dai, L. Wang, Z. He, Perovskite enables high performance vanadium redox flow battery, Chem. Eng. J. 443 (2022) 136341, https://doi.org/10.1016/j.cej.2022.136341.
[16] A.M. Demeku, D.M. Kabtamu, G.-C. Chen, Y.-T. Ou, Z.-J. Huang, N.-Y. Hsu, H.-H. Ku, Y.-M. Wang, C.-H. Wang, High-entropy oxide of $(BiZrMoWCeLa)O_2$ as a novel catalyst for vanadium redox flow batteries, ACS Appl. Mater. Interfaces 16 (2024) 10019–10032, https://doi.org/10.1021/acsami.3c15783.
[17] R. Huang, S. Liu, Z. He, W. Zhu, G. Ye, Y. Su, W. Deng, J. Wang, Electron-deficient sites for improving V^{2+}/V^{3+} redox kinetics in vanadium redox flow batteries, Adv. Funct. Mater. 32 (2022) 2111661, https://doi.org/10.1002/adfm.202111661.
[18] H. He, Q. Zhang, H. Wang, H. Zhang, J. Li, Z. Peng, Y. Tang, M. Shao, Defect-rich TiO2-δ nanocrystals confined in a mooncake-shaped porous carbon matrix as an advanced Na ion battery anode, J. Power Sources 354 (2017) 179–188, https://doi.org/10.1016/j.jpowsour.2017.04.035.
[19] G. Kresse, J. Furthmüller, Efficiency of ab-initio total energy calculations for metals and semiconductors using a plane-wave basis set, Comput. Mater. Sci 6 (1996) 15–50, https://doi.org/10.1016/0927-0256(96)00008-0.
[20] P.E. Blöchl, Projector augmented-wave method, Phys. Rev. B 50 (1994) 17953, https://doi.org/10.1103/physrevb.50.17953.
[21] M. Ernzerhof, G.E. Scuseria, Assessment of the Perdew–Burke–Ernzerhof exchange-correlation functional, J. Chem. Phys. 110 (1999) 5029–5036, https://doi.org/10.1063/1.478401.
[22] S. Grimme, J. Antony, S. Ehrlich, H. Krieg, A consistent and accurate ab initio parametrization of density functional dispersion correction (DFT-D) for the 94 elements H-Pu, J. Chem. Phys. 132 (2010), https://doi.org/10.1063/1.3382344.
[23] D. Guan, H. Xu, Q. Zhang, Y.C. Huang, C. Shi, Y.C. Chang, X. Xu, J. Tang, Y. Gu, C. W. Pao, Identifying a universal activity descriptor and a unifying mechanism concept on perovskite oxides for green hydrogen production, Adv. Mater. 35 (2023) 2305074, https://doi.org/10.1002/adma.202305074.
[24] W. Li, H. Xu, H. Zhang, F. Wei, L. Huang, S. Ke, J. Fu, C. Jing, J. Cheng, S. Liu, Tuning electron delocalization of hydrogen-bonded organic framework cathode for high-performance zinc-organic batteries, Nat. Commun. 14 (2023) 5235, https://doi.org/10.1038/s41467-023-40969-5.
[25] W. Xiao, K. Yoo, J.H. Kim, H. Xu, Breaking barriers to high-practical Li-S batteries with isotropic binary sulfiphilic electrocatalyst: creating a virtuous cycle for favorable polysulfides redox environments, Adv. Sci. 10 (2023) 2303916, https://doi.org/10.1002/advs.202303916.
[26] Q. Zheng, H. Xu, Y. Yao, J. Dai, J. Wang, W. Hou, L. Zhao, X. Zou, G. Zhan, R. Wang, K. Wang, L. Zhang, Cobalt single-atom reverse hydrogen spillover for efficient electrochemical water dissociation and dechlorination, Angew. Chem. Int. Ed. 63 (2024), https://doi.org/10.1002/anie.202401386 e202401386.
[27] K. Mathew, V. Kolluru, S. Mula, S.N. Steinmann, R.G. Hennig, Implicit self-consistent electrolyte model in plane-wave density-functional theory, J. Chem. Phys. 151 (2019), https://doi.org/10.1063/1.5132354.
[28] E. Sanville, S.D. Kenny, R. Smith, G. Henkelman, Improved grid-based algorithm for Bader charge allocation, J. Comput. Chem. 28 (2007) 899–908, https://doi.org/10.1002/jcc.20575.
[29] H. Yuan, S.A.A.A. Aljneibi, J. Yuan, Y. Wang, H. Liu, J. Fang, C. Tang, X. Yan, H. Cai, Y. Gu, ZnO nanosheets abundant in oxygen vacancies derived from metal-organic frameworks for ppb-level gas sensing, Adv. Mater. 31 (2019) 1970076, https://doi.org/10.1002/adma.201807161.
[30] M. Xiao, L. Zhang, B. Luo, M. Lyu, Z. Wang, H. Huang, S. Wang, A. Du, L. Wang, Molten-salt-mediated synthesis of an atomic nickel co-catalyst on TiO_2 for improved photocatalytic H_2 evolution, Angew. Chem. Int. Ed. 132 (2020) 7297–7301, https://doi.org/10.1002/ange.202001148.
[31] Y. Yang, S. Zhao, F. Bi, J. Chen, Y. Wang, L. Cui, J. Xu, X. Zhang, Highly efficient photothermal catalysis of toluene over Co_3O_4/TiO_2 pn heterojunction: The crucial roles of interface defects and band structure, Appl. Catal. B Environ., 315 (2022) 121550, https://doi.org/10.1016/j.apcatb.2022.121550.
[32] K. Qian, Y. Yan, S. Xi, T. Wei, Y. Dai, X. Yan, H. Kobayashi, S. Wang, W. Liu, R. Li, Elucidating the strain–vacancy–activity relationship on structurally deformed Co@CoO nanosheets for aqueous phase reforming of formaldehyde, Small 17 (2021) 2102970, https://doi.org/10.1002/smll.202102970.
[33] M. Zhang, Y. Wang, Y. Zhang, J. Song, Y. Si, J. Yan, C. Ma, Y.T. Liu, J. Yu, B. Ding, Conductive and elastic TiO_2 nanofibrous aerogels: a new concept toward self-supported electrocatalysts with superior activity and durability, Angew. Chem. Int. Ed. 59 (2020) 23252–23260, https://doi.org/10.1002/anie.202010110.
[34] T. Wu, H. Zhao, X. Zhu, Z. Xing, Q. Liu, T. Liu, S. Gao, S. Lu, G. Chen, A.M. Asiri, Y. Zhang, X. Sun, Identifying the origin of Ti^{3+} activity toward enhanced electrocatalytic N_2 reduction over TiO_2 nanoparticles modulated by mixed-valent copper, Adv. Mater. 32 (2020) 2000299, https://doi.org/10.1002/adma.202000299.
[35] Q. Gan, H. He, K. Zhao, Z. He, S. Liu, S. Yang, Plasma-induced oxygen vacancies in urchin-like anatase titania coated by carbon for excellent sodium-ion battery anodes, ACS Appl. Mater. Interfaces 10 (2018) 7031–7042, https://doi.org/10.1021/acsami.7b13760.
[36] Q. Gan, H. He, Y. Zhu, Z. Wang, N. Qin, S. Gu, Z. Li, W. Luo, Z. Lu, Defect-assisted selective surface phosphorus doping to enhance rate capability of titanium dioxide for sodium ion batteries, ACS Nano 13 (2019) 9247–9258, https://doi.org/10.1021/acsnano.9b03766.
[37] M. Yang, H. Li, F. Liu, S. Sun, J. Mei, Y. Jiao, J. Cui, Y. Xu, H. Song, Z. Duan, Mechanism insight into oxygen vacancy-dependent effect in Fe_1/TiO_2 single-atom catalyst for highly enhanced photo-Fenton mineralization of phenol, Appl. Catal. B Environ. Energy 354 (2024) 124071, https://doi.org/10.1016/j.apcatb.2024.124071.
[38] H.-S. Kim, J.B. Cook, H. Lin, J.S. Ko, S.H. Tolbert, V. Ozolins, B. Dunn, Oxygen vacancies enhance pseudocapacitive charge storage properties of MoO_{3-x}, Nat. Mater. 16 (2017) 454–460, https://doi.org/10.1038/nmat4810.
[39] Q. Cheng, M. Huang, L. Xiao, S. Mou, X. Zhao, Y. Xie, G. Jiang, X. Jiang, F. Dong, Unraveling the influence of oxygen vacancy concentration on electrocatalytic CO_2 reduction to formate over indium oxide catalysts, ACS Catal. 13 (2023) 4021–4029, https://doi.org/10.1021/acscatal.2c06228.s001.
[40] W. Huang, K. Zhang, B. Yuan, L. Yang, M. Zhu, Predominant intercalation of H^+ enables ultrahigh rate capability of oxygen deficient MoO_3 for aqueous Al-ion batteries, Energy Storage Mater. 50 (2022) 152–160, https://doi.org/10.1016/j.ensm.2022.05.016.
[41] X. Wei, C. Chen, X.Z. Fu, S. Wang, Oxygen vacancies-rich metal oxide for electrocatalytic nitrogen cycle, Adv. Energy Mater. 14 (2024) 2303027, https://doi.org/10.1002/aenm.202303027.
[42] L. Tang, T. Li, W. Lu, X. Li, Reversible solid bromine complexation into $Ti_3C_2T_x$ MXene carriers: a highly active electrode for bromine-based flow batteries with ultralow self-discharge, Energ. Environ. Sci. 17 (2024) 3136–3145, https://doi.org/10.1039/D4EE00580E.
[43] W. Ling, C. Nie, X. Wu, X.-X. Zeng, F. Mo, Q. Ma, Z. Lu, G. Luo, Y. Huang, Ion Sieve Interface Assisted Zinc Anode with High Zinc Utilization and Ultralong Cycle Life for 61 Wh/kg Mild Aqueous Pouch Battery, ACS Nano 18 (2024) 5003–5016, https://doi.org/10.1021/acsnano.3c11115.
[44] M. Ding, H. Fu, X. Lou, M. He, B. Chen, Z. Han, S. Chu, B. Lu, G. Zhou, C. Jia, A stable and energy-dense polysulfide/permanganate flow battery, ACS Nano 17 (2023) 16252–16263, https://doi.org/10.1021/acsnano.3c06273.
[45] X. Zhang, A. Valencia, W. Li, K. Ao, J. Shi, X. Yue, R. Zhang, W.A. Daoud, Decoupling activation and transport by electron-regulated atomic-Bi harnessed surface-to-pore interface for vanadium redox flow battery, Adv. Mater. 36 (2024) 2305415, https://doi.org/10.1002/adma.202305415.
[46] G. Ye, S. Liu, K. Zhao, Z. He, Singlet oxygen induced site-specific etching boosts nitrogen-carbon sites for high-efficiency oxygen reduction, Angew. Chem. Int. Ed. 135 (2023), https://doi.org/10.1002/anie.202303409 e202303409.
[47] W. Ma, T. Liu, C. Xu, C. Lei, P. Jiang, X. He, X. Liang, A twelve-electron conversion iodine cathode enabled by interhalogen chemistry in aqueous solution, Nat. Commun. 14 (2023) 5508, https://doi.org/10.1038/s41467-023-41071-6.
[48] L. Zhou, W. Zhou, H. Wang, Q. Deng, X. Ai, X.-X. Zeng, X. Wu, C. Zhou, W. Ling, In-situ constructed interface buffer layer enabled highly reversible Zn Deposition/Stripping for long-lifespan aqueous zinc metal anodes, Chem. Eng. J. 492 (2024) 152324, https://doi.org/10.1016/j.cej.2024.152324.

[49] R. Huang, S. Liu, Z. He, G. Ye, W. Zhu, H. Xu, J. Wang, The role of proton in high power density vanadium redox flow batteries, ACS Nano 17 (2023) 19098–19108, https://doi.org/10.1021/acsnano.3c05037.
[50] Y. Gao, J. He, H. Guo, Modeling and detection of small electron polaron: a comparison between bond distortion method and occupation matrix control method, J. Phys. Chem. C 128 (2024) 5244–5256, https://doi.org/10.1021/acs.jpcc.3c07206.s001.
[51] Y. Li, S. Yang, Y. Zhao, N. Mubarak, M. Xu, M. Ihsan-Ul-Haq, T. Zhao, Q. Chen, J.-K. Kim, Deciphering the exceptional kinetics of hierarchical nitrogen-doped carbon electrodes for high-performance vanadium redox flow batteries, J. Mater. Chem. A 10 (2022) 5605–5613, https://doi.org/10.1039/d2ta00324d.
[52] X. Zhang, L. Liu, S. Hou, Q. Zhou, Y. Zhang, X. Chen, N. Pu, J. Liu, C. Yan, Nitrogen, phosphorus, and sulfur co-doped carbon nanotubes/melamine foam composite electrode for high-performance vanadium redox flow battery, J. Mater. Sci. Technol. 190 (2024) 127–134, https://doi.org/10.1016/j.jmst.2023.12.029.
[53] J. Ye, L. Xia, H. Li, F.P.G. de Arquer, H. Wang, The critical analysis of membranes towards sustainable and efficient vanadium redox flow batteries, Adv. Mater. 36 (2024) 2402090, https://doi.org/10.1002/adma.202402090.